COMMUNICATION

Check for updates

An 'antifouling' porous loofah sponge with internal microchannels as solar absorbers and water pumpers for thermal desalination†

Chao Liu, [ID] Kevin Hong, Xiao Sun, Avi Natan, Pengcheng Luan, Yang Yang and Hongli Zhu [ID] *

As a new solar technology, interface steam generation has great prospects in the application of desalination and fractionation. Herein, we report a sustainable, efficient, and accessible loofah-based solar evaporator with a bilayer structure. The top carbonized layer functioned as efficient solar absorbers with broad light absorption and high light trapping. At the bottom layer, attributed to loofah fibers' natural hydrophilicity and hierarchical macropores and microchannels, sufficient water was pumped to the localized heating interface. During desalination, the salt concentration gradient between the macropores and microchannels allowed for efficient salt drainage in the loofah and prevented the accumulation of salt on the surface of the evaporator, thus ensuring long-term stability. This economical light absorber and the water-pumping natural fibers exhibited a steam generation rate of $\sim$1.42 kg m^{-2} h^{-1} and an efficiency of 89.9% under one Sun. This low cost, abundant, and stable material is promising for future large-scale solar steam applications.

1. Introduction

Water pollution and freshwater shortages are becoming global issues that warrant serious consideration. Water desalination and purification from seawater or wastewater represent cost-effective methods for addressing the globally growing need for clean water.[1,2] Many advances have been explored in obtaining pure water, such as the development of reverse osmosis technologies, membrane treatments, ion exchange, and some multi-effect distillation systems.[3–6] Compared with these high-cost technologies, which are ultimately unsustainable, solar-driven evaporation has drawn tremendous attention because it uses abundant solar energy and has a small environmental footprint.[7] The major factors affecting solar evaporation are broadband light adsorption, heat localization, water supply,

and water evaporation.[2,6,8] Conventional sunlight absorbers, some of the novel designs, have been considered for water supply and solar absorption, including carbon-based materials with strong light absorption,[9–11] heat localizing plasmonic nanoparticles,[4,12,13] and hydrophilic sponges with carbonized surfaces.[14–16] However, challenges persist in the use of solar steam generators, including: (1) their relatively low energy conversion efficiencies due to heat dissipation throughout the volume of the liquid; (2) their often expensive materials and complicated fabrication processes, which limit their large-scale application; (3) the insufficient supply of water from bulk water to the evaporative surface for continuous steam generation; (4) salt accumulation induced efficiency decay.[2,5,14,17–19]

On the other hand, over the past century, humankind benefited from the consumer convenience and technological advancements enabled by petroleum-based plastics, while at the same time perpetuating the negative consequences of non-degradable plastic wastes after their service life. To increase the sustainability of human society, new strategies for materials synthesis and a focus on renewable resources is needed. To this end, nature provides abundant raw materials that can be transformed into biodegradable and high-performance multi-functional materials. These biologically derived materials and structures are readily distinguished from synthesized materials by their naturally unique characteristics. Their long-term sustainability is the most attractive feature and has garnered the attention of many researchers. Recently, natural materials were used to fabricate solar evaporators, including carbonized wood,[19–22] sugarcane stems,[23] and mushrooms,[24] which can efficiently generate vapor and transport water. Hu et al. made great progress using both hard- and softwood-based evaporators. A wood-based evaporator that prevented salt accumulation has also been developed by punching holes in wood.[22] However, the evaporation rate under 1 Sun of irradiance was only $\sim$1 kg m^{-2} h^{-1} and its evaporation efficiency is between 70 and 80%, which is relatively lower than that of the materials obtained from the market, such as carbon felt[25] and carbon fiber clothes.[26] Liu et al.[23] reported that when using a surface-

Department of Mechanical and Industrial Engineering, Northeastern University, Boston, Massachusetts 02115, USA. E-mail: h.zhu@neu.edu

† Electronic supplementary information (ESI) available. See DOI: 10.1039/d0ta03872e

carbonized sugarcane stem as a solar steam generator, the evaporative efficiency was up to 87.4% under 1 Sun of irradiance. Meanwhile, Xu et al.[24] employed the unique natural structure of a mushroom to enable solar steam generation with an evaporative conversion efficiency of 78%. The major challenge with wood is the low evaporation rate and efficiency due to limited water transfer paths at unit volume and a consequent low water absorption rate. The major issue of sugarcane and mushroom works is that the salt accumulation problem was ignored during desalination by using pure water other than saltwater. Also the mechanism of light absorption and trapping lacks in-depth understanding, which is critical for optimizing solar efficiency in solar steam.

Loofahs, in the form of widely available dried "sponges," are a sustainable and cost-efficient biomass derived from the fruit of loofah plants. They are commonly used as cleaning tools.[27,28] As a light-weight natural material, loofah sponges also have the potential to be used as an alternative material for various engineering applications (e.g., packaging, energy storage, water absorption).[29–31] In chemistry, a loofah sponge is mainly composed of cellulose (60–65 wt%),[32] which is highly hydrophilic. At the same time, the loofah fibers form the percolated three-dimensional (3D) porous structure and there are abundant well-aligned microchannels inside each loofah fiber. Based on this unique hierarchical structure, a loofah sponge has superior water absorption properties. In this study, for the first time, we designed bilayer loofah sponges, the blackened top layer and native bottom layer, with highly efficient light and water absorption as sustainable and stable solar evaporators. In the top layer, we found that the black rough loofah fiber surface serves an antireflection function. Meanwhile, the light is trapped between the layered porous meshes. The well aligned microchannels inside each fiber increased the light transfer paths and therefore increased the light trapping. Owing to the broad-spectrum light absorbing and trapping at the carbonized layer, favorably interconnected microchannels for water transport, high heat localization, and efficient interface salt exchange, the evaporation rate and conversion efficiency of the loofah-based evaporator reached up to 1.42 kg m^{-2} h^{-1} and 89.9% under 1 Sun, respectively. Interestingly, the salt concentration gradient of the macropores and microchannels allowed the macropores to act as salt drains, while the high water absorption of the loofah sponge further diluted the salt in the upper micro-channels. Therefore, this high-efficiency solar evaporator, which has antifouling properties, has broad prospects for large-scale applications.

2. Experimental

2.1 Material preparation

Dried loofahs were purchased from a local market. The loofah-based evaporator was made by cutting the natural loofahs into a cylindrical shape with a diameter of 50 mm and a thickness of 10 mm. The surface layer was carbonized at 500 °C for 30 s by using a hotplate to form a uniform carbonized layer.

2.2 Characterization

The morphology and structure of the loofah-based evaporator were characterized by scanning electron microscopy (SEM, Hitachi S4800, Hitachi Ltd., Japan). The water absorption rate of the material was obtained by immersing wood and loofahs in deionized water for 1 h and calculating the weight ratio of the materials before and after absorption. Fourier-transform infrared spectroscopy (FT-IR) was conducted using a VERTEX FTIR 70 (Bruker Corp., USA). The reflection and transmission properties of the sample were measured by using an ultraviolet-visible near infrared (UV-vis-NIR) spectrophotometer (Cary 5000, Agilent Technologies Inc., USA). The absorbance (A) of the sample was calculated based on the reflectance (R) and transmittance (T) obtained, such that $A = 1 - R - T$. Thermographic images were captured using an infrared thermal camera (HT-18, Dongguan Xintai Instrument, China) with a thermal sensitivity of ≤0.05 °C. Thermal conductivity of the dry and wet loofah sponges was tested by using a Hot Disk TPS 2500s instrument (Hot Disk AB, Sweden) with 20 mW output power at room temperature. X-ray diffractometry (XRD) measurements were conducted on an X'pert PRO system (Malvern Panalytical, Germany) using Cu Kα radiation at 40 kV and 30 mA.

2.3 Solar steam generation experiments

The solar steam generation experiments were measured using a standard solar simulator (HSX-F300, NBeT, China). Solar power was simulated using a light intensity receiver (NBeT VLP-2000). The loofah-based evaporator was placed in a water-filled beaker and mass change data were collected by an electronic balance with an accuracy of 0.1 g. The photothermal conversion efficiency was calculated using the following formula:

$$\eta = \dot{m}h_{\mathrm{LV}}/C_{\mathrm{opt}}q_{\mathrm{i}} \tag{1}$$

where $\dot{m}$ is the evaporation rate under different illumination conditions, subtracting the evaporation rate in the dark field and the contribution of the supporter. Additionally, h_{LV} represents the evaporative enthalpy, including both the sensible and latent heat of the phase change; C_{opt} is the optical concentration and q_{i} is the standard solar radiation.

3. Results and discussion

Loofah sponges are abundant resources from loofah fruits and are widely cultivated in tropical countries across Asia and Africa, as well as in some subtropical regions. Photographs of the loofah fruit are shown in Fig. 1A. Due to the shallowness of the native loofah sponge's natural color, the native loofah sponge's solar absorption in the broad-spectrum is limited. To optimize the loofah sponge for solar-driven evaporation, a carbonization process was applied to blacken the surface layer, and therefore dramatically increase light absorption at the top layer (Fig. 1B and S1†). Compared to the non-integrated double layered structures,[26] our integrated bilayer structure can eliminate the gap between the two layers to minimize the water and thermal transfer resistance. The resultant evaporator displayed an
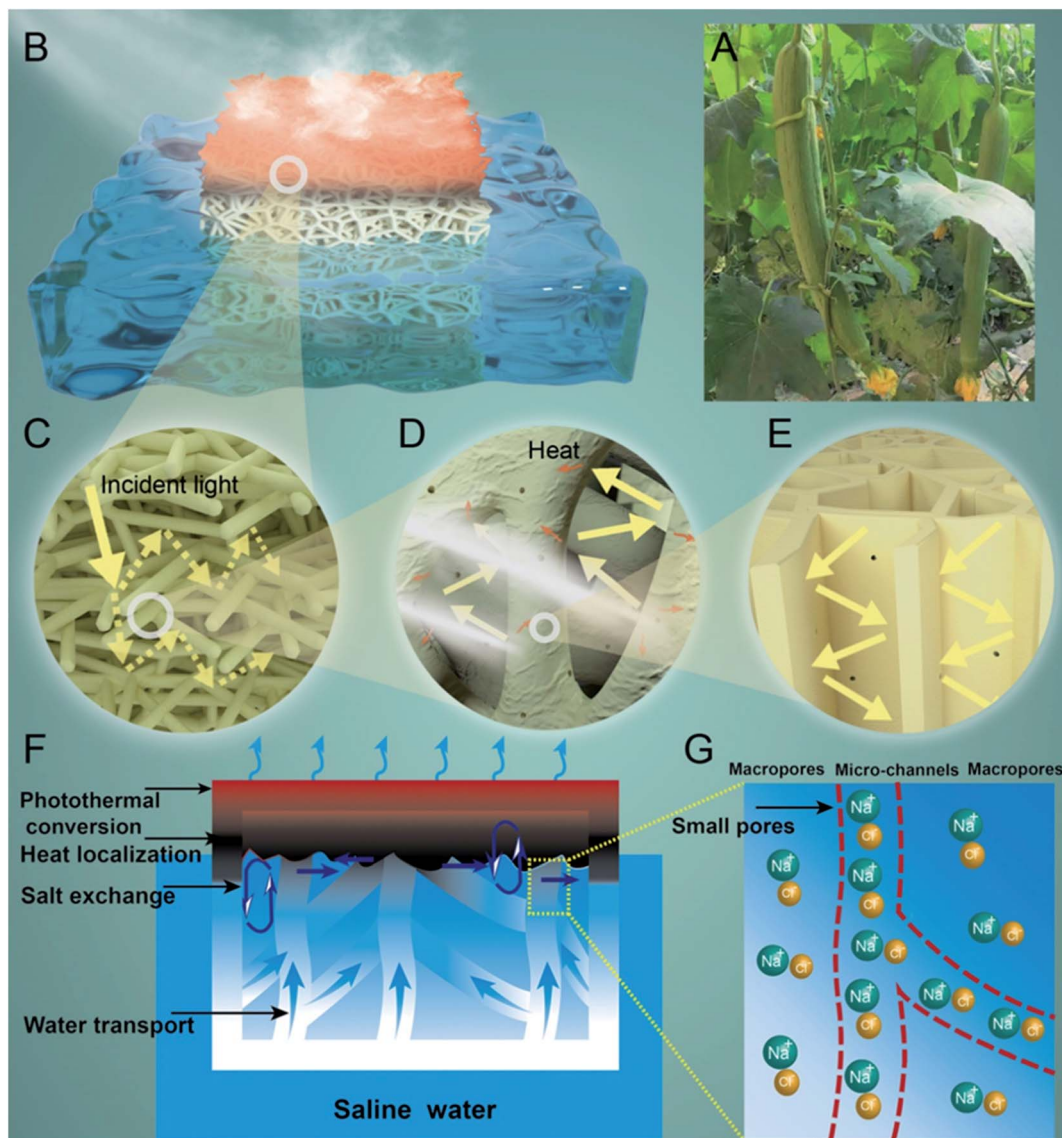
Fig. 1 Loofah plant and its solar thermal desalination mechanism in detail. (A) Photograph of the loofah plant. A schematic illustration of (B) a loofah-based solar steam generation device can be prepared on a large scale by using a surface carbonized loofah sponge; the heating layer was used for light adsorption and loofah microchannels constantly pump sea water. A schematic illustration depicting the light absorption mechanism of (C) the multilayer structure of the evaporator; (D) the macropores of the evaporator; (E) the microchannels of the evaporator. Mechanism of mass transfer in the evaporator (F) the evaporator has several characteristics such as interconnected microchannels for vapor transportation, the broad-spectrum light absorption carbonized surface as well as the heat localization properties and interface salt exchange. (G) The salt concentration gradient between the microchannels and the macropores enabled salt exchange to prevent salt accumulation.

integrated structure with a carbonized layer of ~2 mm on the top surface for light adsorption and an untreated natural layer of ~8 mm at the bottom of the evaporator.

The light absorption mechanism of our solar evaporator is shown in Fig. 1B–E. Compared to the flat and dense structure, the interconnected porous structure composed of coarse fibers further increases light absorption through light trapping, anti-reflection, and increasing surface area. There are three primary mechanisms for light trapping: (1) in Fig. 1C, the multilayer structure causes internal light to be scattered and trapped in the limited space between the layers; (2) in Fig. 1D, the incident light undergoes multiple reflections inside the macropores, at the micro scale, formed between fibers; (3) as shown in Fig. 1E,

the microchannels inside fibers maximize the light absorption by trapping light inside the channels.

On the one hand, the highly hydrophilic loofah cellulose fibers with abundant hydroxyl groups can absorb water quickly. On the other hand, combining the physical hydrophilicity and micro-channels, the surface of the infiltrating liquid in the capillary is concave, which exerts a capillary tensile force on the liquid below, causing the liquid to rise along the microchannel wall. The hydrophilic fibers and their internal microchannel structures provided sufficient water supply by transporting water to the heating surface through capillary action (Fig. 1F). The water absorbed to the heat localized surface keeps evaporating, which causes the tension and gravity of the liquid difficult to balance

and maintain running cycles. Furthermore, the water can be transferred to the heat localization surface from different directions through the connected pores at the micro scale.

During seawater desalination, the continuous evaporation of water on the upper surface will inevitably lead to an increase in salt concentration at the localized heating surface. As shown in Fig. 1G, the salt concentration in the microchannels will be much higher than macropores in the sponge because of the limited water amount in microchannels, resulting in a horizontal salt concentration gradient. The salt concentration distribution is ordered as: upper layer microchannels > upper layer macropores > lower layer microchannels > lower layer macropores. The salt concentration gradient led to salt exchange between the microchannels and the 3D porous structure of the sponge. Meanwhile, in the vertical direction, high-salinity water in the upper layer spontaneously exchanges with low-salinity water in the lower layer to dilute the salt concentration in the upper layer (Fig. 1F). Additionally, the loofah sponge's excellent hydrophilicity quickly absorbs water to complement the vaporized brine at the heating surface to avoid salt accumulation. The inherent porous structure of the fiber and its microchannels solve the salt accumulation spontaneously.

Fig. 2A and S2† are the digital images of the native loofah sponge, from which we can see the 3D porous structure formed
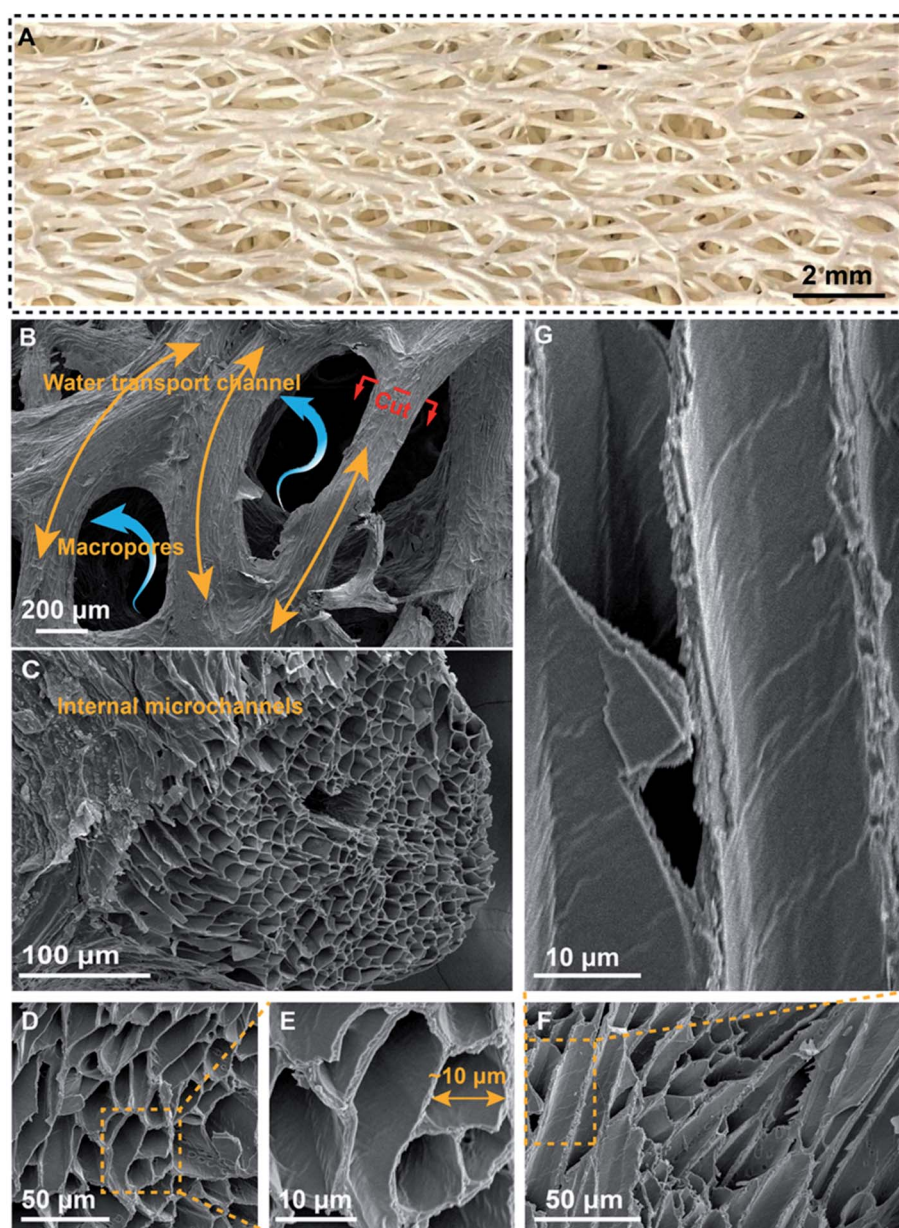

Fig. 2 Morphological and structural characterization of the loofah-based evaporator. (A) Photographs showing the geometrical features of the loofah sponge. (B) SEM images showing the 3D porous structure and internal channels of the evaporator. (C) SEM images showing the cross-sectional view of a loofah fiber, which illustrate the multi-microchannel structure inside the fiber. (D and E) SEM images showing the channel structure at different magnifications. (F and G) Along-channel SEM images showing interlaced channels at different magnifications.

between fibers and the different layers possessing different porosity. The zoomed in morphology and structure of the loofah sponge are further characterized by scanning electron microscopy (SEM). As shown in Fig. 2B, the upper layer of the evaporator still retains its original shape after carbonization. The upper carbonized layer has an interconnected porous structure, which benefit light transportation. Unlike a flat surface that depends on the angle of the incident light, the cylindrical coarse fiber surface increases the specific surface area of light absorption to a greater extent. The effective absorption of sunlight can be maintained throughout the day. The multilayered structure extends the multi-scattered optical path and reduces the reflectivity, which contributes to the ultra-high light absorption capacity of the evaporator. The macropores formed among the fibers facilitate light-trapping. The incident light undergoes multiple reflections inside macropores and microchannels, which maximizes the light absorbed by the material and generates heat. Fig. 2C illustrates the unique microchannel structure inside the fiber, which facilitates light trapping. Fig. 2D–G show the zoomed in channel structure of the evaporator. The channels are arranged continuously and the diameters of the channels range from 10–20 μm. The well defined channels extended in the direction of the coarse fibers (Fig. 2F and G).

The SEM images of the bottom layer are presented in Fig. S3.† A multitude of microchannels were arranged in each of the coarse fibers, which ensured rapid vapor transportation during solar evaporation (Fig. S3A†). Fig. S3B and C† are magnified SEM images of the cross section and longitudinal section of the microchannels. There are small holes on the walls of these microchannels that connect the channels. These interconnected microchannels allow absorbed water to be transported to the evaporation surface from multiple directions. The pictures of fibers with different magnifications are shown in Fig. S3D–F.† Interestingly, there were also holes distributed across the surface of the loofah fibers (Fig. S3E and F†), which enabled salt exchange and prevented salt accumulation during solar evaporation.

The mechanical stability of an evaporator is an essential factor for its long-time usage. As shown in Fig. 3A, the loofah sponge exhibited excellent mechanical strength. A 4.5 g loofah sponge was able to withstand 6 kg of water in the direction of the outer wall – 1300 times more than its own weight – without deformation. Additionally, it was able to bend in any direction without breaking and maintained its original shape very well. Thus it can be flexibly reshaped to maximize the contact area with the water surface. The water absorption capacity of the loofah sponge is calculated by the mass of the water absorbed per unit in the loofah sponge at a unit time and presented in Fig. 3B. The water absorption rate of the loofah sponge reaches 16.2 g g^{-1}, which is approximately seven times higher than that of balsa wood. The inset in Fig. 3B also shows the excellent water absorption of the loofah sponge. Compared with balsa wood, the high water absorption of the loofah is partly due to the swelling of the fiber and its porous structure, making it highly absorbent.
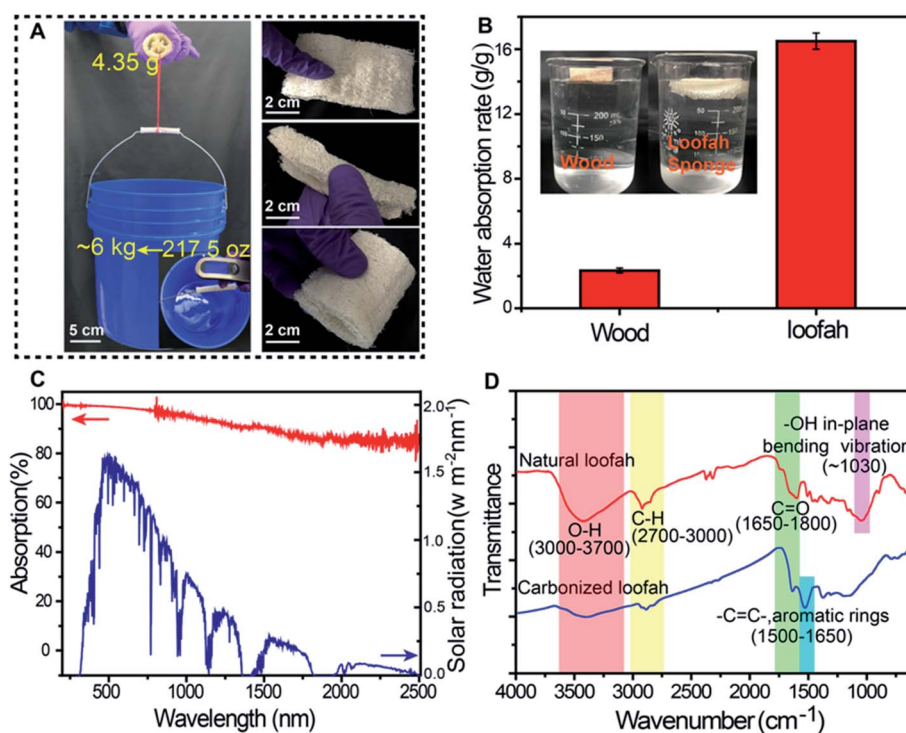

Fig. 3 Mechanical robustness, water absorption rate, light absorption, and surface functional group characterization of the loofah. (A) Photographs of the robust performance of the loofah sponge. (B) Water absorption properties of a loofah sponge and wood. (C) Absorption spectra of the carbonized loofah sponge (red) and solar radiation in an ambient environment (blue). (D) FT-IR spectra of the natural (red) and carbonized loofah sponges (blue).

In order to investigate the broadband photo-absorption ability of the carbonized loofah sponge over a range of 200–2500 nm, an ultraviolet-visible-near infrared (UV-vis-NIR) spectrophotometer was used to measure the optical absorption of the evaporator. As shown in Fig. 3C and S4,† the loofah-based evaporator exhibited high optical absorption (∼98.60%) in the ultraviolet and visible light regions (200–780 nm) and ∼92.13% absorption in the near-infrared region (780–2500 nm). Overall, the evaporator exhibited an average light absorption of ∼95.4% across the broadband wavelength, making it promising to harvest solar energy to the utmost extent for photo-thermal conversion in a solar steam power generator. In contrast, the natural loofah sponge exhibited a low average light absorption (∼48.4%) across the broadband wavelength (Fig. S5†). The excellent optical absorption properties of the loofah-based evaporator were primarily attributed to light scattering in the carbonized fibers and porous structure. Furthermore, the thermal conductivity of the dry loofah sponge and wet loofah sponge was investigated (Fig. S6†). The pristine dry loofah sponge shows a low thermal conductivity of 57.5 mW m^{-1} K^{-1} and the wet loofah sponge has a thermal conductivity of 62.0 mW m^{-1} K^{-1}. Thus, the bottom sponge-like porous structure of the loofah was effectively co-opted as a heat insulator to prevent the downward diffusion of heat due to its low thermal conductivity. The functional groups of the natural loofah sponge (bottom layer) and the carbonized loofah sponge (top layer) were investigated using Fourier-transform infrared (FTIR) spectra (Fig. 3D). Compared to the bottom layer, the O–H groups (O–H stretching vibration and hydrogen bond in the hydroxyl group) at 3000–3700 cm^{-1} and –OH groups (C–O stretching vibration in cellulose/hemicellulose) at ∼1030 cm^{-1} verified that the disappearance of most of the hydroxyl groups in the top layer was due to carbonization. Attenuation of the signal peak intensities for the C–H bond at 2700–3000 cm^{-1} and the increase of –C=C– (1500–1650 cm^{-1}) of the carbonized loofah illustrated the formation of more carbon-to-carbon bonding, which facilitated light absorption.[22]

The solar-driven evaporative capabilities of our loofah-based evaporator were measured by the mass change of water in a beaker under 1, 2, 3, and 5 Sun of irradiation at a room temperature of 20 °C and a humidity of 40% (Fig. S7†). Meanwhile, by optimizing the evaporator of the carbonized layer with different thicknesses, the evaporator with a thickness of 2 mm carbonized layer had the most stable performance (Fig. S8†). Upon irradiation, the water was rapidly evaporated, with generation of steam over the loofah-based evaporator (Fig. 4A and S9†). The schematic of the solar-driven steam generator is shown in Fig. 4B. The evaporator was placed in a container that could float on water without any auxiliary equipment. A well-balanced combination of broadband light adsorption, heat localization, water supply, and water evaporation ensured the high evaporation rate and conversion efficiency. The mass changes of water, the natural loofah sponge/water, the top surface carbonized wood/water, and the loofah-based evaporator/water under 1 Sun of illumination are shown in Fig. 4C. Due to the unique 3D porous structure, the integrated design and the microchannels that act as capillaries in the fibers of the loofah sponge, its evaporative ability was 1.42 kg m^{-2} h^{-1}, which is much higher than those of the natural loofah sponge (0.45 kg m^{-2} h^{-1}) or wood based evaporator (0.82 kg m^{-2} h^{-1}) (Fig. S10†). The natural loofah sponge has less solar absorption due to the shallowness of its natural color and the unidirectional wood channels. These interconnected microchannels allow water absorption to be transported to the evaporator surface from different directions, which further promotes the evaporation of water. To exclude the influence of pure water evaporation, the pure water evaporation rate was also investigated. The evaporation rate of the loofah-based evaporator was found to be 6.5 times greater than that of pure water (0.22 kg m^{-2} h^{-1}).

The evaporation rate of the loofah-based evaporator under a high optical concentration was further examined (Fig. 4D). Increased solar illumination led to higher evaporation rates, which were maximized at 6.62 kg m^{-2} h^{-1} under 5 Sun (5 kW m^{-2}); the conversion efficiencies under different illumination intensities were 89.9%, 92.0%, 90.1%, and 90.7% for 1, 2, 3, and 5 Sun, respectively (Fig. 4E). Meanwhile, we have theoretically estimated the related energy loss of the loofah based evaporator at 1 Sun illumination in the ESI,† from which we found that the total energy consumption by the water evaporator is about 87.8%. This number is close to the steam generation efficiency of 89.9%. Interestingly, the trend of evaporative efficiency change was inconsistent with the evaporation rate change. This phenomenon was attributed to the high sun concentration, which led to the water evaporating faster than the water being transported to the surface, causing heating diffusion to the air and side paths.[26] The cycling performance of the evaporator was also investigated under solar illuminations of 1, 2, 3, and 5 Sun, with each cycle sustained over 1 h (Fig. 4F). The evaporator presented a stable evaporation rate, indicating its superior reusability. Overall, the loofah sponge-based evaporator in this study exhibited superior performance to those previously reported for biologically derived materials and other photo-thermal materials under 1 Sun of illumination. A detailed comparison of the relevant data is shown in Fig. 4G and Table S1.†[20,21,24,33–39] The evaporation rate and evaporation efficiency of this work is at the top. Furthermore, the design is low-cost and can be easily scaled up for practical applications compared with the reported literature.

The light absorption of the loofah-based evaporator was investigated using an infrared (IR) camera. Fig. 5 shows the temperature gradient of the carbonized loofah sponge (CLS) in water, pure water, and the dry carbonized loofah sponge in the ambient environment over time. For the beaker with a CLS and water (Fig. 5A), the temperature rose rapidly in the first 5 min and then stabilized at ∼63 °C after 30 min. For this setup, the highest temperature region was on the top (carbonized) surface throughout the process, while the (natural) bottom remained at room temperature. Heat was localized on the surface because the thermal conductivity of the loofah sponge was as low as ∼0.06 W m^{-1} K^{-1}.[40] A material with a low thermal conductivity has a lower rate of heat transfer, which explains why the temperature was significantly higher at the surface of the carbonized loofah sponge while the water below it remained
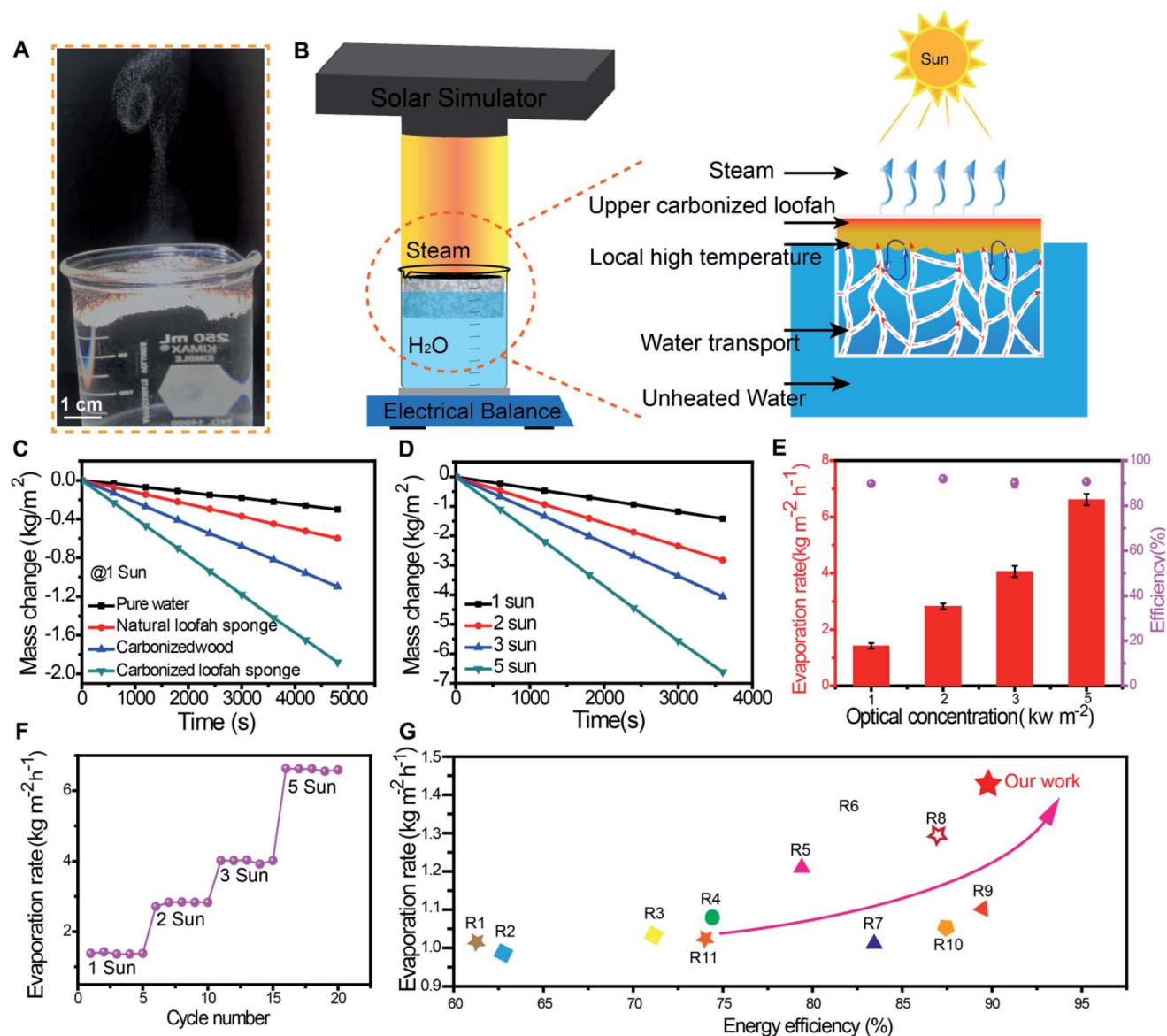
Fig. 4 Setup of the loofah-based evaporator and characterization of loofah water evaporation performance. (A) Photograph of visible vapor generated under 3 Suns of illumination. (B) Illustration of the solar water evaporation experimental setup. (C) Mass changes of water using pure water, the natural loofah sponge, carbonized wood, and the carbonized loofah sponge under 1 Sun of illumination individually. (D) Mass changes of the carbonized loofah sponge under solar illuminations of 1, 2, 3 and 5 kW m^{-2}. (E) Efficiency and evaporation rate under solar illuminations of 1, 2, 3, and 5 kW m^{-2}. (F) Cycling performance of water evaporation on the carbonized loofah sponge under a solar illumination of 1, 2, 3, and 5 kW m^{-2}, with each cycle sustained over 1 h; the correlation between the evaporation rate and optical concentration are linear. (G) Loofah-based evaporator steam production compared with previous reports under 1 Sun; detailed data are listed in Table S1.†

nearly unchanged even after exposure. In contrast, for the beaker containing only water (Fig. 5B), the top surface temperature rose slowly over time and the entire system exhibited a homogeneous temperature distribution. We also tested the distribution of temperature over time for a dried carbonized loofah sponge (DCLS) (Fig. 5C). Under the illumination of 3 Sun, the surface temperature of the DCLS rose rapidly to ~115 °C in 1 min, which demonstrated its excellent light–thermal conversion efficiency. These results suggest that high light-absorption and heat localization can be achieved in this system due to the unique structure and design of the CLS.

For practical desalination applications, the cycling and stability of an evaporator are challenging because of the long exposure time to solar radiation. For unstable materials, surface salt crystallization severely hinders the rate of evaporation and conversion efficiency during solar desalination. Also most of the refractory, carbon-based materials and plasmonic metals previously reported are costly, which is not ideal for practical applications. The salt precipitated on the top of evaporators dramatically decreases their performance, especially in highly salt-concentrated solutions.[22] As shown in Fig. 6A, under the condition of a 20% salt concentration and 1 Sun of
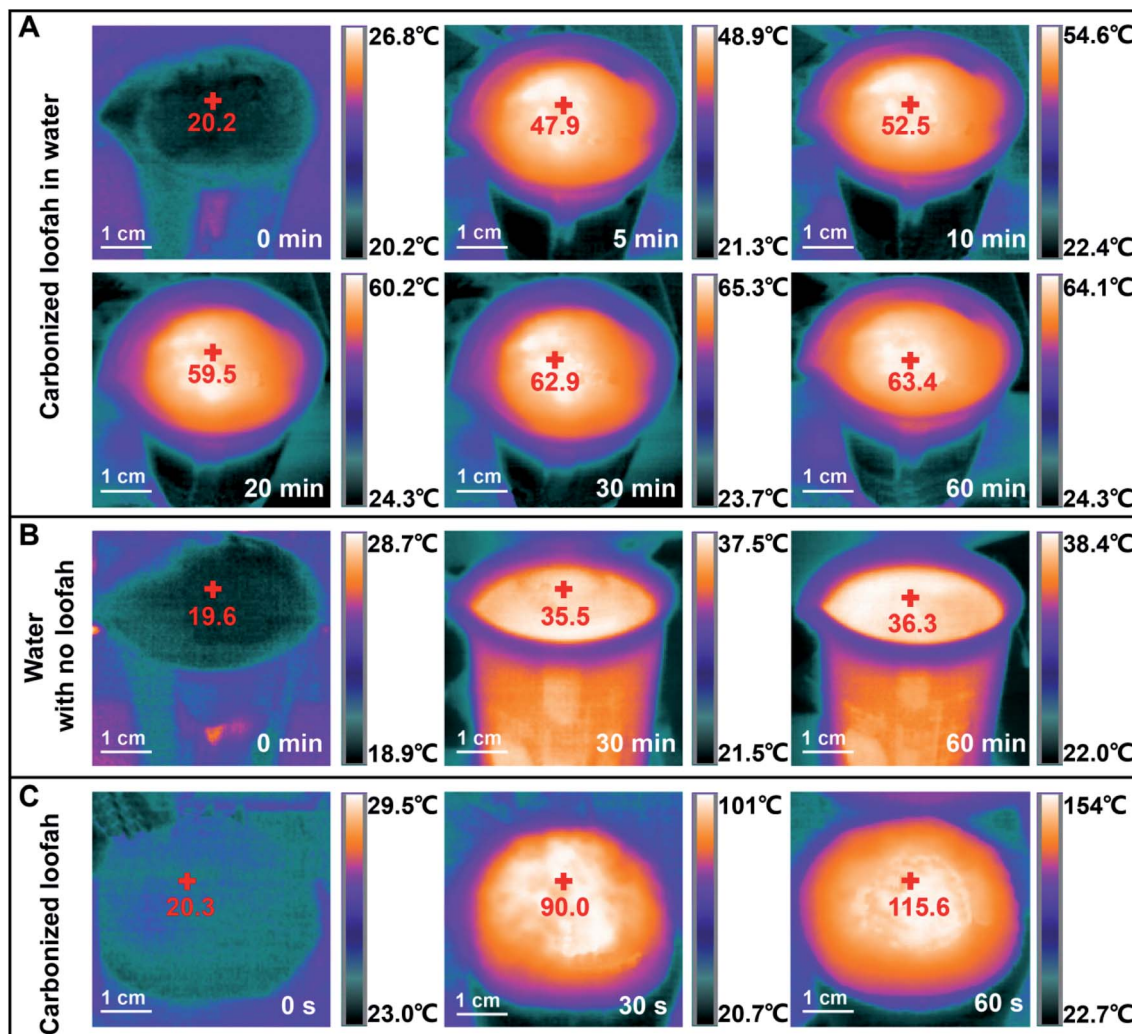
Fig. 5 Images of temperature distributions by using an IR camera for the carbonized loofah sponge in water and pure water, and the dry carbonized loofah sponge. (A) Surface temperature evolution of a carbonized loofah sponge in water under 3 Sun of illumination after 0, 5, 10, 20, 30, and 60 min. (B) Surface temperatures of pure water under 3 Sun of illumination after 0, 30, and 60 min. (C) Surface temperatures of the dry carbonized loofah sponge under 3 Sun of illumination after 0, 30, and 60 s.

illumination, salt deposition occurred on the surface of carbon felt after 2 h and salt accumulation overtime was more severer. In contrast, there was no obvious salt accumulation on the top of the CLS. Due to the influence of surface salt crystallization, the evaporation rate of carbon felt decreased from 0.96 kg m^{-2} h^{-1} to 0.61 kg m^{-2} h^{-1} ($\sim$36%). However, under the same conditions of a 20% salt concentration and 1 Sun of illumination, the evaporation rate of CLS was basically stable at $\sim$1.25 kg m^{-2} h^{-1} (Fig. 6B). Further, to investigate salt accumulation, carbon felt and the carbonized loofah sponge after 10 hours evaporation in 20% salt concentration seawater are observed with SEM (Fig. S11 and S12†). Fig. S11A† shows the precipitated salt on top of the carbon felt evaporator after 1 h. Fig. S11B and C† are magnified SEM images of A, which show salt accumulated on the carbon felt surface. These accumulated salts could severely affect evaporating performance. As shown in Fig. S11D,† once the salt water on the fiber surface reaches the saturation point due to the rapid evaporation of water during

operation, salt crystals were observed starting from the carbon fiber and then gradually spreading over the carbon felt surface. Compared with the carbon felt fiber with salt accumulation, pristine carbon felt fiber shows a clean surface (Fig. S11E and F†). In contrast, there was no obvious salt accumulation on the loofah fiber surface and internal microchannels (Fig. S12†). This antifouling behavior was attributed to the salt concentration gradient between the hierarchical 3D porous structure and microchannels of the CLS. The top layer of the microchannels freely exchanges water with the macropores. Additionally, the high-salinity water in the upper layer spontaneously exchanges with the low-salinity water in the lower layer to dilute the salt concentration in the upper layer. Meanwhile, the good hydrophilicity of the loofah sponge quickly complemented the surface moisture of the vaporized brine.

We investigated the effects of salt concentrations on the evaporation rate of the loofah-based evaporator, as shown in Fig. 6C. The evaporation rate decreased from 1.42 kg m^{-2} h^{-1}
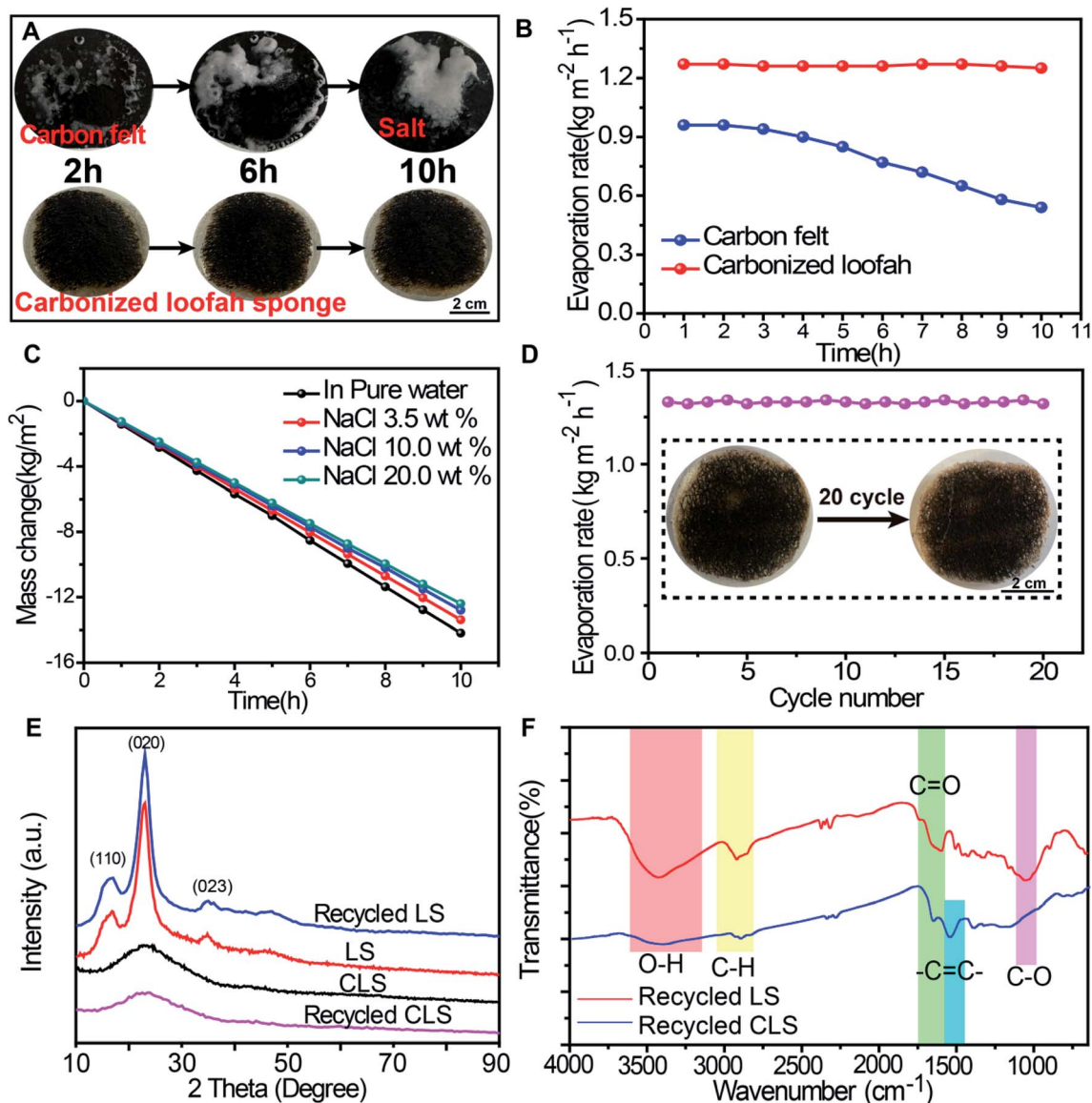
Fig. 6 Stability and physicochemical properties of biologically derived evaporators. (A) Photograph showing salt-blockages at the surface of a conventional carbon felt evaporator and no salt-blockages at the surface of the carbonized loofah sponge after 10 h in a 20% NaCl solution with a solar irradiance of 1 Sun. (B) Evaporation rate of a carbon felt and carbonized loofah evaporator with a solar irradiance of 1 Sun over time. (C) Mass change of the carbonized loofah based evaporator at different salt concentrations over time. (D) Evaporation rate as a function of the number of cycles. Inset is the photograph of a carbonized loofah sponge before and after cycling to show the stability of its shape. (E) XRD spectra of the top (carbonized) layer of a loofah sponge, natural loofah sponge, recycled loofah sponge, and recycled carbonized loofah sponge. (F) FT-IR spectra of the loofah sponge and recycled carbonized loofah sponge.

for pure water to 1.3 kg m^{-2} h^{-1} for a 10% salt concentration and 1.25 kg m^{-2} h^{-1} for a 20% salt concentration, which demonstrates the stability of the CLS in practical seawater desalination applications. Fig. 6D further shows the cycling performance of the CLS in a simulated seawater system with an average evaporation rate of 1.33 kg m^{-2} h^{-1}, where the concentration of salt was controlled at ~3.5% for each cycle under 1 Sun of illumination for more than 20 days with a 5 h illumination per cycle per day (totally > 100 h). There was no obvious degradation or damage to the CLS evaporator (inset of Fig. 6D). The X-ray diffraction (XRD) and FTIR spectra were also used to illustrate the stability of the cycled CLS. As shown in

Fig. 6E, the diffraction peaks at 15.7°, 22.9°, and 34.4° at the curves of recycled LS and LS corresponded to the typical (110), (002), and (023) planes of cellulose I. The broad diffraction peak appeared at ~22° at the curves of CLS and recycled CLS, revealing the low crystalline structure of the top layer of CLS and recycled CLS. The original and recycled loofah-based evaporators exhibited similar structures with respect to their diffraction patterns, indicating that the structure of the evaporator does not change during the repeated operation process for longer than 100 h. From the FTIR spectra (Fig. 6F), the absorption peaks at ~3400 and 1050 cm^{-1} were characteristic of cellulose and were attributed to the stretching vibration of O–H in

hydroxyl groups and C–O groups, respectively. The peak at ~2905 cm^{-1} showed the presence of C–H and CH$_2$, which are the characteristic peaks in cellulose and hemicellulose. The peak at 1500–1650 cm^{-1} (C=C stretching vibration in benzene rings and stretching vibration of C=C with a conjugated C–C bond) were derived from lignin. The top layer and bottom layer of the evaporator that was recycled several times retained their molecular structures after being reused.

From the XRD and FTIR results of the recycled CLS, we can see that the loofah is stable under UV radiation. Commercial sponge materials made from petroleum, such as polyurethane (PU) are easily oxidized and unstable under long-term exposure of xenon light. As shown in Fig. S13,† a PU sponge coated with carbon black was used in solar evaporation for 5 Sun for 3 h. The PU sponge had good water absorption, but a collapse in the center of the PU sponge was observed, which seriously affected its water evaporation efficiency and its long term stability. The loofah sponge's ultraviolet light stability and broad-spectrum absorption of light are important for solar evaporation applications.

4. Conclusions

In this work, we used a hydrophilic loofah derived from nature with a unique hierarchical structure of one microfiber (~100 μm) composed with well aligned microchannels (10–20 μm) as the light absorber and water pumper for solar desalination. By a ready surface carbonization treatment, an integrated bilayer structure with no interface resistance was obtained. Attributed to a multilayered structure and the extension of the multi-scattered optical path, incident light undergoes multiple reflections inside the macropores, as well as the light trapping inside the microchannels; the top carbonized layer of the loofah sponge acted as an excellent photothermal material with the ability to absorb solar energy at a broad spectrum. The unique 3D macroporous structure, well aligned microchannels, and sufficient hydroxyl groups of the loofah sponge ensured high water absorption. The evaporation rate and conversion efficiency could reach up to 1.42 kg m^{-2} h^{-1} and 89.9%, respectively, under 1 Sun of illumination. The bilayer loofah outperformed most previously studied biologically derived photothermal materials. Simultaneously, the salt concentration gradient between the microchannels and the 3D macropores led to salt exchange between the microchannels and macropores to prevent salt accumulation and maintain the performance. More importantly, the loofah is chemically and physically stable under solar illumination. Our findings suggest that abundant, sustainable, and low-cost loofah sponges from nature can be applied for solar steam generation and the integrated design of loofah-based evaporators may allow for the development of sustainable, durable, and scalable solar desalination systems in the near future.

Author contributions

Data and materials availability

All data needed to evaluate the conclusions in the paper are present in the paper and/or the Supplementary Materials. Additional data related to this paper may be requested from the authors.

Conflicts of interest

There are no conflicts to declare.

Acknowledgements

References

1 X. Han, W. Wang, K. Zuo, L. Chen, L. Yuan, J. Liang, Q. Li, P. M. Ajayan, Y. Zhao and J. Lou, *Nano Energy*, 2019, **60**, 567–575.

2 X. Zhou, F. Zhao, Y. Guo, Y. Zhang and G. Yu, *Energy Environ. Sci.*, 2018, **11**, 1985–1992.

3 X. Chen and N. Y. Yip, *Environ. Sci. Technol.*, 2018, **52**, 2242–2250.

4 Y. Liu, S. Yu, R. Feng, A. Bernard, Y. Liu, Y. Zhang, H. Duan, W. Shang, P. Tao and C. Song, *Adv. Mater.*, 2015, **27**, 2768–2774.

5 K. Bae, G. Kang, S. K. Cho, W. Park, K. Kim and W. J. Padilla, *Nat. Commun.*, 2015, **6**, 10103.

6 G. Ni, G. Li, S. V. Boriskina, H. Li, W. Yang, T. Zhang and G. Chen, *Nat. Energy*, 2016, **1**, 16126.

7 N. S. Lewis, *Science*, 2016, **351**, aad1920.

8 H. Jin, G. Lin, L. Bai, A. Zeiny and D. Wen, *Nano Energy*, 2016, **28**, 397–406.

9 L. Sun, J. Liu, Y. Zhao, J. Xu and Y. Li, *Carbon*, 2019, **145**, 352–358.

10 Z. Yin, H. Wang, M. Jian, Y. Li, K. Xia, M. Zhang, C. Wang, Q. Wang, M. Ma and Q.-s. Zheng, *ACS Appl. Mater. Interfaces*, 2017, **9**, 28596–28603.

11 H. Ghasemi, G. Ni, A. M. Marconnet, J. Loomis, S. Yerci, N. Miljkovic and G. Chen, *Nat. Commun.*, 2014, **5**, 4449.

12 O. Neumann, A. S. Urban, J. Day, S. Lal, P. Nordlander and N. J. Halas, *ACS Nano*, 2012, 7, 42–49.

13 N. J. Hogan, A. S. Urban, C. Ayala-Orozco, A. Pimpinelli, P. Nordlander and N. J. Halas, *Nano Lett.*, 2014, **14**, 4640–4645.

14 P. Zhang, J. Li, L. Lv, Y. Zhao and L. Qu, *ACS Nano*, 2017, **11**, 5087–5093.

15 P. Zhang, Q. Liao, T. Zhang, H. Cheng, Y. Huang, C. Yang, C. Li, L. Jiang and L. Qu, *Nano Energy*, 2018, **46**, 415–422.

16 Y. Yang, R. Zhao, T. Zhang, K. Zhao, P. Xiao, Y. Ma, P. M. Ajayan, G. Shi and Y. Chen, *ACS Nano*, 2018, **12**, 829–835.

17 Y. Li, T. Gao, Z. Yang, C. Chen, W. Luo, J. Song, E. Hitz, C. Jia, Y. Zhou and B. Liu, *Adv. Mater.*, 2017, **29**, 1700981.

18 L. Zhou, Y. Tan, D. Ji, B. Zhu, P. Zhang, J. Xu, Q. Gan, Z. Yu and J. Zhu, *Sci. Adv.*, 2016, **2**, e1501227.

19 S. He, C. Chen, Y. Kuang, R. Mi, Y. Liu, Y. Pei, W. Kong, W. Gan, H. Xie and E. Hitz, *Energy Environ. Sci.*, 2019, **12**, 1558–1567.

20 C. Chen, Y. Li, J. Song, Z. Yang, Y. Kuang, E. Hitz, C. Jia, A. Gong, F. Jiang and J. Zhu, *Adv. Mater.*, 2017, **29**, 1701756.

21 G. Xue, K. Liu, Q. Chen, P. Yang, J. Li, T. Ding, J. Duan, B. Qi and J. Zhou, *ACS Appl. Mater. Interfaces*, 2017, **9**, 15052–15057.

22 Y. Kuang, C. Chen, S. He, E. M. Hitz, Y. Wang, W. Gan, R. Mi and L. Hu, *Adv. Mater.*, 2019, 1900498.

23 J. Liu, Q. Liu, D. Ma, Y. Yuan, J. Yao, W. Zhang, H. Su, Y. Su, J. Gu and D. Zhang, *J. Mater. Chem. A*, 2019, **7**, 9034–9039.

24 N. Xu, X. Hu, W. Xu, X. Li, L. Zhou, S. Zhu and J. Zhu, *Adv. Mater.*, 2017, **29**, 1606762.

25 Z. Yu, S. Cheng, C. Li, L. Li and J. Yang, *ACS Appl. Mater. Interfaces*, 2019, **11**, 32038–32045.

26 Q. Fang, T. Li, H. Lin, R. Jiang and F. Liu, *ACS Appl. Energy Mater.*, 2019, **2**, 4354–4361.

27 Y. Yuan, S. Zhou, Y. Liu and J. Tang, *Environ. Sci. Technol.*, 2013, **47**, 14525–14532.

28 I. Oboh and E. Aluyor, *Afr. J. Agric. Res.*, 2009, **4**, 684–688.

29 H. Demir, U. Atikler, D. Balköse and F. Tıhmınlıoğlu, *Composites, Part A*, 2006, **37**, 447–456.

30 I. O. Oboh, E. O. Aluyor and T. O. Audu, *Waste Water-Treatment and Reutilization*, InTech, 2011, pp. 195–212.

31 D. Xie, X.-h. Xia, W.-j. Tang, Y. Zhong, Y.-d. Wang, D.-h. Wang, X.-l. Wang and J.-p. Tu, *J. Mater. Chem. A*, 2017, **5**, 7578–7585.

32 Y. Wang, Z.-x. Ding, Y.-h. Zhang, C.-y. Wei and Z.-c. Xie, *Polymers*, 2019, **11**, 37.

33 Y. Wang, L. Zhang and P. Wang, *ACS Sustainable Chem. Eng.*, 2016, **4**, 1223–1230.

34 S. MohammadáSajadi and S. HiáWang, *J. Mater. Chem. A*, 2017, **5**, 15227–15234.

35 A. Guo, X. Ming, Y. Fu, G. Wang and X. Wang, *ACS Appl. Mater. Interfaces*, 2017, **9**, 29958–29964.

36 Y. Li, T. Gao, Z. Yang, C. Chen, Y. Kuang, J. Song, C. Jia, E. M. Hitz, B. Yang and L. Hu, *Nano Energy*, 2017, **41**, 201–209.

37 H. Ren, M. Tang, B. Guan, K. Wang, J. Yang, F. Wang, M. Wang, J. Shan, Z. Chen and D. Wei, *Adv. Mater.*, 2017, **29**, 1702590.

38 X. Wang, Y. He, X. Liu, G. Cheng and J. Zhu, *Appl. Energy*, 2017, **195**, 414–425.

39 H. Li, Y. He, Y. Hu and X. Wang, *ACS Appl. Mater. Interfaces*, 2018, **10**, 9362–9368.

40 P. Daniel and K. Yadav, *International Journal of Scientific Research and Management*, 2016, **4**, 4514–4524.